RSC Advances

ROYAL SOCIETY OF CHEMISTRY

PAPER

View Article Online
View Journal | View Issue

Check for updates

Cite this: *RSC Adv.*, 2025, **15**, 14183

Turning mango kernel waste into high-energy porous carbon: a sustainable electrode material for high-performance supercapacitors with exceptional stability

Vandana Molahalli, †*[ab] Vinay S. Bhat, †*[c] Aman Sharma, [de] Gowri Soman[de] and Gurumurthy Hegde *[de]

Received 26th March 2025
Accepted 23rd April 2025

DOI: 10.1039/d5ra02129d

rsc.li/rsc-advances

This study explores the sustainable production of high-performance supercapacitor electrodes from waste mango kernels, addressing the growing need for eco-friendly energy storage solutions. Porous carbon materials were synthesized *via* pyrolysis at varying temperatures (700, 800, 900, and 1000 °C), designated as MK7, MK8, MK9, and MK10, respectively. The synthesized carbon was obtained *via* a simple and eco-friendly carbonization, yielding a highly porous structure with a large specific surface area of 1348.9 m^2 g^{-1}, for MK9 material as confirmed by BET analysis. Raman spectroscopy revealed a high degree of graphitization with D and G bands, indicating the presence of both disordered and graphitic carbon domains. SEM imaging showed a well-developed, interconnected porous morphology, while XRD patterns confirmed the amorphous nature with partially crystalline domains. The resulting carbon materials were evaluated for their electrochemical performance in supercapacitor applications. Electrochemical characterization revealed that the MK9 sample, pyrolyzed at 900 °C, exhibited the highest specific capacitance of 205.8 F g^{-1}, surpassing the performance of the other samples. To optimize device performance, symmetric supercapacitors were fabricated using a CR2032 coin cell configuration with different electrolytes and concentrations. The KOH electrolyte device demonstrated a maximum power density of 5137.86 W kg^{-1}, an energy density of 12.32 W h kg^{-1}, and a specific capacitance of 112.4 F g^{-1}. Furthermore, this device exhibited excellent cycling stability, maintaining its performance over 100 000 galvanostatic charge–discharge cycles. A practical demonstration showed the ability of the device to power a red LED for approximately 15 minutes. These results highlight the potential of utilizing waste biomass, specifically mango kernels, for sustainable and efficient supercapacitor development.

1. Introduction

Growing energy demands and environmental challenges necessitate developing sustainable, high-performance energy storage solutions. Supercapacitors offer a promising alternative due to their advantages, including fast charge–discharge capabilities, high power density, extended cycle life, and environmentally benign nature.[1,2] However, the difficulty in producing high-performance electrode materials that are both cost-effective and sustainable impedes the broader implementation of supercapacitors. As a result, reusing bio-waste in applications that store electricity is desirable as a waste management and environmental protection strategy.[3] Traditional energy storage predominantly relies on fuel cells, batteries, and capacitors. However, to address the growing demand for clean energy, a more integrated approach combining energy storage and conversion systems, such as batteries, supercapacitors, fuel cells, and solar cells, is essential.[4] Due to their excellent rate capability, remarkable stability, rapid charge/discharge process, high power density, and long cycle life,[5,6] supercapacitors, also called electrochemical double-layered capacitors, or EDLCs, have drawn much attention recently.

Compared to other carbonaceous precursors, biomass can be easily turned into carbon.[7] It is a naturally occurring resource that is abundant on earth, recyclable, and has a very permeable structure. Porous carbon compounds are known for their high

---

[a] *Department of Physics, B. M. S. College of Engineering, Bengaluru, 560019, India*

[b] *Centre for Nano-Materials & Displays, B. M. S. College of Engineering, Bengaluru, 560019, India. E-mail: vandanam254@gmail.com*

[c] *Department of Physics, Mangalore University, Mangalagangotri, 574199, India. E-mail: s.vinaybhat@gmail.com*

[d] *Department of Chemistry, School of Sciences, Christ University, Bengaluru, Karnataka, 560029, India*

[e] *Centre for Advanced Research and Development (CARD), Christ University, Bengaluru, Karnataka, 560029, India. E-mail: murthyhegde@gmail.com*

† Equally contributed to the manuscript.

surface area and conductivity, making them ideal for supercapacitor electrodes.[8] Porous carbons are commercially produced from petroleum by-products using either templated or non-templated methods. Materials such as siliceous sources, clays, zeolites, and other inorganic substances have been employed as templates.[9–12] The non-templated approach generates hierarchical porous carbons with topological structures similar to those obtained through template-based methods but at a lower cost and in a single-step process.[13] Carbon materials synthesized from agricultural waste biomass are increasingly attracting attention for supercapacitor applications because of their high surface area and hierarchical porosity, which make them highly suitable for efficient energy storage. Biomass or biowaste materials like garlic peel,[13] onion peel,[14] banana peel,[15] *Caesalpinia sappan* pods,[16] *Arachis hypogaea* skin,[17] *Lablab purpureus* seeds,[18] orange peel,[19] oil palm leaves[20] and walnut shell,[21] *etc.* have been utilized as carbon precursors, offering an efficient approach to convert biomass waste into valuable products. However, there are no reports of using mango kernels for the same.

Mango (*Mangifera indica*) is a prominent tropical fruit crop primarily cultivated for its edible pulp. The seed, accounting for 20–60% of the fruit's total weight, is often discarded in mango-producing regions due to its minimal culinary and commercial applications. With limited utilization globally, mango kernels represent an underexplored resource, with an estimated 18 to 22 million tonnes generated annually.[22] Mango by-products present significant environmental and economic concerns for the food industry and the broader community. Globally, approximately 123 000 metric tonnes of mango seeds are discarded annually, adding to the waste generated by the fruit processing sector. The seed accounts for 20–60% of the total fruit mass, with the kernel comprising 45–75% of the seed weight.[3,23,24] During mango fruit processing, approximately 40–60% of the waste generated primarily consists of mango kernels. Its lignocellulosic structure comprises approximately 25.2% cellulose, 34.06% hemicellulose, and 15.0% lignin.[25] Considering its abundance and underutilization, we identified mango kernels as a viable precursor for synthesizing porous carbon nanomaterials (PCNs). Despite the potential of biomass-derived carbon materials, research on mango seed-derived porous carbon for supercapacitors is rare.

This work used a simple, one-step, non-activated carbonization process to create porous hard carbon from biowaste mango kernel. Different carbonization temperatures ranging from 700 °C (MK7) to 1000 °C (MK10) were employed to examine the electrochemical performance and physicochemical characteristics. Porous carbon from mango kernels were used for the first time in a supercapacitor application to assess electrochemical performance. This offers a sustainable approach to waste management while contributing to advancements in renewable energy storage technology.

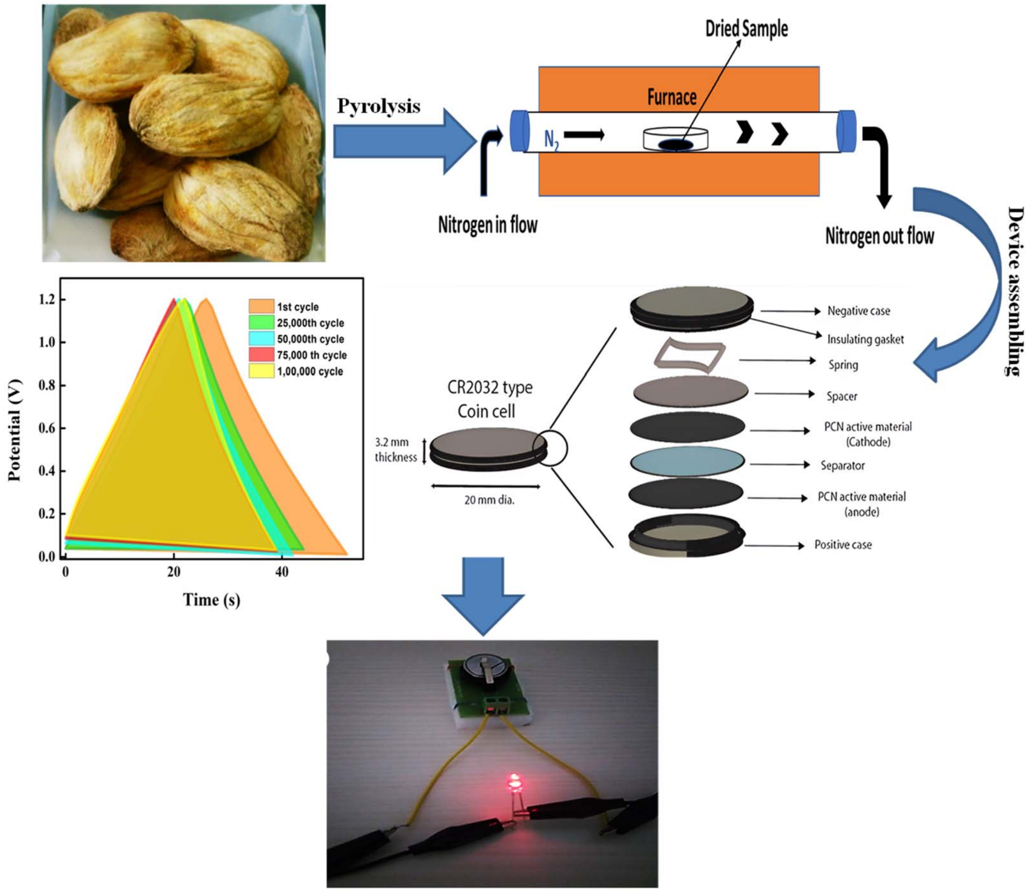

Fig. 1 Schematic diagram of synthesis of porous carbon materials from pyrolysis and supercapacitor device study.

Symmetric CR2032-type supercapacitors were fabricated using various electrolytes (Fig. 1), and their energy performance was compared with previously reported studies, demonstrating superior results. Therefore, the main objective of this study is to develop a sustainable, high-performance porous carbon material derived from mango kernel waste for use as an efficient electrode in supercapacitors, focusing on optimizing its structural properties, electrochemical performance, and long-term cycling stability.

The biomass-derived carbon materials have been widely studied, but the use of mango kernels (a highly abundant yet underutilized agro-waste) as a precursor for porous carbon in supercapacitor electrodes remains significantly unexplored. Despite the huge generation of mango seed waste (∼123 000 metric tons), there are no prior reports on utilizing mango kernels specifically for porous carbon synthesis in energy storage applications. In addition, several studies employ chemical activation to enhance porosity, while the present study demonstrates that a simple, controlled thermal pyrolysis of mango kernels under N_2 atmosphere is sufficient to generate a high surface area with excellent specific capacitance. This proves that activation is not always essential when the precursor itself (with high lignocellulosic content) naturally provides hierarchical porosity upon thermal treatment. Moreover, by avoiding activating agents, we reduce environmental processing complexity.

2. Experimental section

2.1. Synthesis of porous carbon from *Mangifera indica* kernels

The dried *Mangifera indica* kernels were powdered and sieved through a 60 μm mesh. The obtained fine powder of the precursor was then subjected to slow pyrolysis, with a heating rate of 10 °C min^{-1} and a cooling rate of 2 °C min^{-1} under N_2 atmosphere. The pyrolysis was carried out at elevated temperatures of 700, 800, 900, and 1000 °C without any activating agents. The obtained porous carbon was labelled MK7, MK8, MK9, and MK10, respectively.

2.2. Fabrication of the working electrode

A working electrode was fabricated by uniformly coating pre-cleaned nickel foam with a mixture of MK, PVDF binder, and carbon black conductive additive in a 90 : 5 : 5 weight ratio, respectively, using *N*-methyl-2-pyrrolidone (NMP) as the solvent. The coated electrode was pressed under the pressure of 100 kg cm^{-2} and dried overnight at 80 °C, yielding a working electrode with an active material loading for the three-electrode system of 2.3, 2.0, 2.61, and 2.73 mg for MK7, MK8, MK9, and MK10, respectively. Electrochemical characterization was carried out in a three-electrode configuration using 3 M KOH as the electrolyte. A saturated calomel electrode (SCE) and a platinum wire were employed as the reference and counter electrodes, respectively. All electrochemical measurements were performed using an AUTOLAB M204 potentiostat/galvanostat equipped with a frequency response analyzer (FRA).

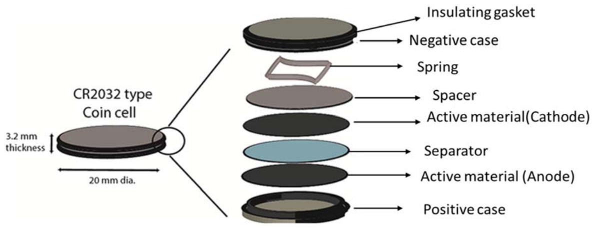

Fig. 2 Components of symmetric CR2032 type device.

Electrochemical analysis included cyclic voltammetry (CV) at scan rates of 10 to 100 mV s^{-1} within a potential range of −1.0 to 0 V *versus* SCE, galvanostatic charge–discharge (GCD) measurements at current densities from 0.1 to 1.0 Ag^{-1}, and electrochemical impedance spectroscopy (EIS) performed across a frequency range of 100 kHz to 0.01 Hz with a 10 mV AC signal at the open circuit potential.

A symmetrical supercapacitor was constructed by coating 2.5 mg of active material onto each of two identical electrodes, separated by a 3.0 M KOH-soaked Whatman glass microfiber filter membrane. The assembled CR2032 coin cell, with a total active material loading of approximately 5 mg, was compressed at 1000 PSI. The symmetrical supercapacitor was then electrochemically characterized under conditions similar to the three-electrode setup. The device assembly is illustrated in Fig. 2.

2.3. Characterization techniques

The morphology and structure of the pyrolyzed carbon were characterized by FESEM-EDS (SEM, Apreo, Thermo Fisher Scientific, India). XRD (Rigaku Model: Smart lab X-ray Diffractometer) was performed from 10° to 80° to determine the crystallinity of the synthesized material. BET and *t*-plot analysis (BELSORP-max, Microtrac, Japan) measured surface area, pore size, and pore volume. The electrochemical investigation of the synthesized porous carbon was studied in (Metrohm AUTOLAB M204, Netherlands) multichannel electrochemical workstation.

3. Results and discussion

3.1. Porosity studies

The surface area of the porous carbon synthesized (MK7, MK8, MK9, and MK10) was better understood by the N_2 Adsorption–desorption isotherm experiment carried out at 77 K, as given in Fig. 3a–e. Except for MK7, all the isotherms exhibit type IVa characteristics, indicating capillary condensation followed by hysteresis. This behavior occurs when pore widths exceed a critical size, which depends on the adsorption mechanism and temperature. The porous carbon ranging from 78 to 710 displays H4-type hysteresis loops. These H4 loops are relatively consistent, with the adsorption branch showing a combination of type I and type II features, primarily due to micropore filling at low p/p_0 values. This suggests that MK7 materials possess a hierarchical porous structure.

According to the BET model, MK9 exhibits the highest specific surface area (SSA) of 1348.5 m^2 g^{-1}. The SSA, pore

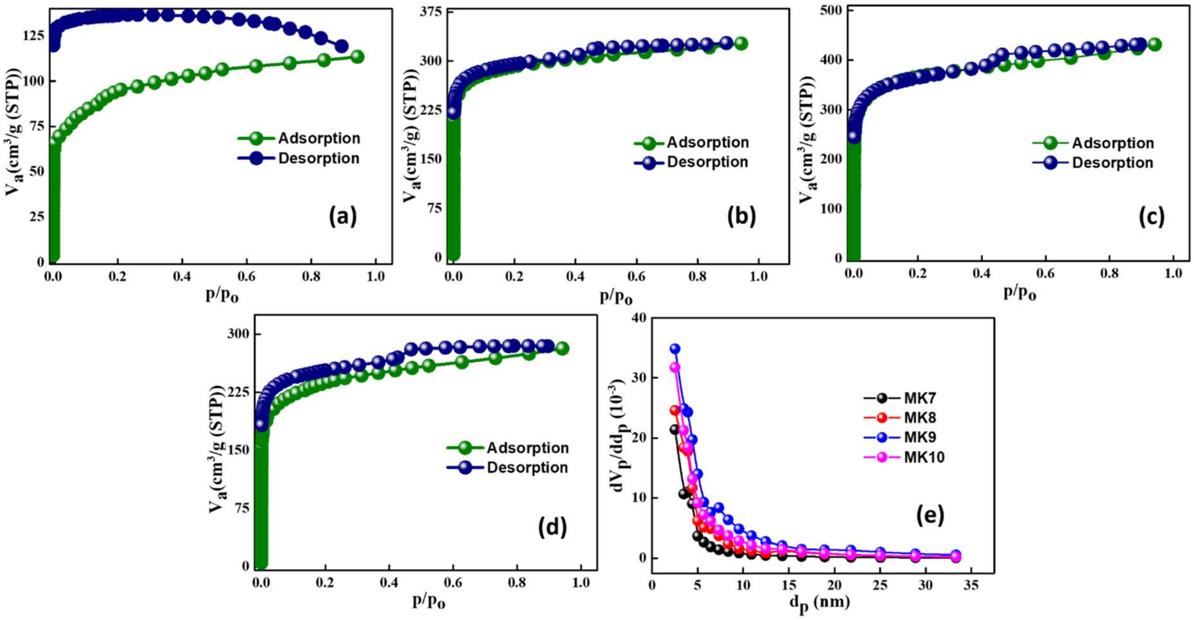

Fig. 3 N_2 adsorption isotherms of MK7 (a), MK8 (b), MK9 (c), MK10 (d), pore size distribution for MK7 materials (e).

Table 1 Porosity data obtained from N_2 adsorption–desorption isotherms for MK samples

Carbon material	BET specific surface area ($m^2\ g^{-1}$)	Total pore volume ($cm^3\ g^{-1}$)	Mean pore diameter (nm)
MK7	330.3	0.18	2.1
MK8	1090.2	0.5	1.9
MK9	1348.5	0.67	1.9
MK10	850.4	0.43	2.0

volume, and pore size for all samples are presented in Table 1, showing a uniform pore size of around 2 nm. Pore size distribution curves (Fig. 3e) further confirm significant gas adsorption in the extensive micropore/small mesopore range, with MK9 showing the highest adsorption, correlating with its larger surface area. At 900 °C, the balance between volatile removal and pore structure formation maximizes the surface area. However, at 1000 °C, excessive heat leads to sintering, graphitization, and partial pore collapse, reducing the surface area.

3.2. FE-SEM analysis

Scanning electron microscopy (SEM) images of the mango kernel-derived carbon samples pyrolyzed at different temperatures (700 °C to 1000 °C) reveal significant morphological evolution with increasing temperature, as shown in Fig. 4a–h. At 700 °C, the carbon material exhibits a relatively smooth surface with limited pore development and shows a sphere-like structure. As the pyrolysis temperature increases to 1000 °C, the surface becomes more porous and rougher, with visible development of micro- and mesopores due to enhanced volatile release and partial structural breakdown. At 1000 °C, the carbon structure shows a well-developed nanosphere, suggesting more extensive decomposition and carbonization. The average diameter of the sphere is nearly 50 nm. This temperature-dependent morphological change directly contributes to improved surface area and ion-accessible sites, which are used for enhanced electrochemical performance in supercapacitor applications. EDS analysis (Fig. 4h inset) confirms a dominant carbon content of 84.86%, along with 10.9% of oxygen and trace amounts of Mg (0.76%), P (1.18%), and K (2.31%) from the biomass precursor. The presence of oxygen and trace elements suggests the biochar retains some of its original biomass characteristics, which can impact its applications.

3.3. XRD and Raman analysis

X-ray diffraction (XRD) analysis of MK9 (Fig. 5a) reveals a broad amorphous (002) peak at $2\theta \approx 25°$, corresponding to a d-spacing between graphene sheets of 3.5 Å, and a (100) peak at 43°, relating to the in-plane graphitic structure. Raman spectroscopy was performed to investigate the structural characteristics and degree of graphitization of the synthesized MK9 carbon material (Fig. 5b).

The Raman spectrum displayed two prominent peaks: the D-band around $\sim$1387 cm^{-1}, which corresponds to disordered carbon or defects in the carbon structure, and the G-band around $\sim$1532 cm^{-1}, which is associated with the graphitic sp^2-hybridized carbon domains. Indicating a partially graphitized structure with a balanced presence of ordered and

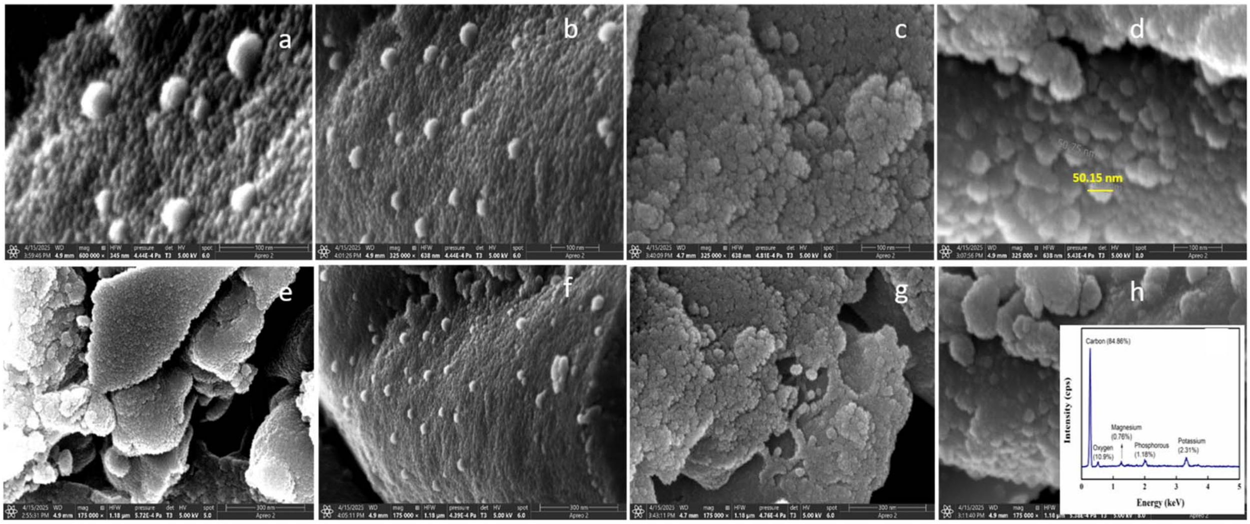

Fig. 4 SEM image of MK7 (a and e), MK8 (b and f), MK9 (c and g), MK10 (d and h) samples at low and high magnifications and EDS plot from SEM (h inset).

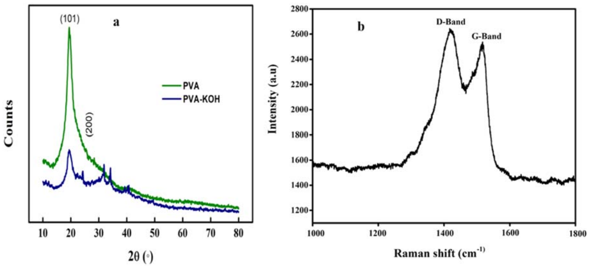

Fig. 5 XRD (a) and RAMAN (b) analysis of MK9.

disordered carbon regions. This structural feature is beneficial for super capacitor applications, as the graphitic domains enhance electrical conductivity, while the disordered regions contribute to ion adsorption and charge storage.

3.4. XPS analysis

X-ray photoelectron spectroscopy (XPS) analysis of MK9 reveals key insights into their surface chemistry and elemental composition. Fig. 6 shows the XPS wide scan spectra of the MK9 sample, containing two prominent peaks corresponding to carbon (binding energy of 284.75 eV) and oxygen (binding energy of 530.89 eV). The primary feature of the XPS spectrum is the intense carbon (C 1s) peak shown in Fig. 6b, which can be deconvoluted into several components, corresponding to different carbon species present on the surface of the nanospheres such as C═O, C–O–C, C–C, C═C groups, which are associated with binding energies in the range of 282–290 eV respectively. The O 1s peak observed in the XPS spectrum, as shown in Fig. 6c, indicates the presence of oxygen-containing surface functionalities, specifically bonds like C═O and O–C═O. This peak reflects the surface oxygen content, which plays a crucial role in determining the surface chemistry of the material. In some cases, trace amounts of nitrogen (N) may also be identified near 398 eV in the wide scan, likely originating from residual components in the mango kernel, with varying percentages. The comparative intensities of the C 1s and O 1s peaks offer insight into the surface carbon-to-oxygen ratio, an important factor in evaluating the chemical reactivity of the

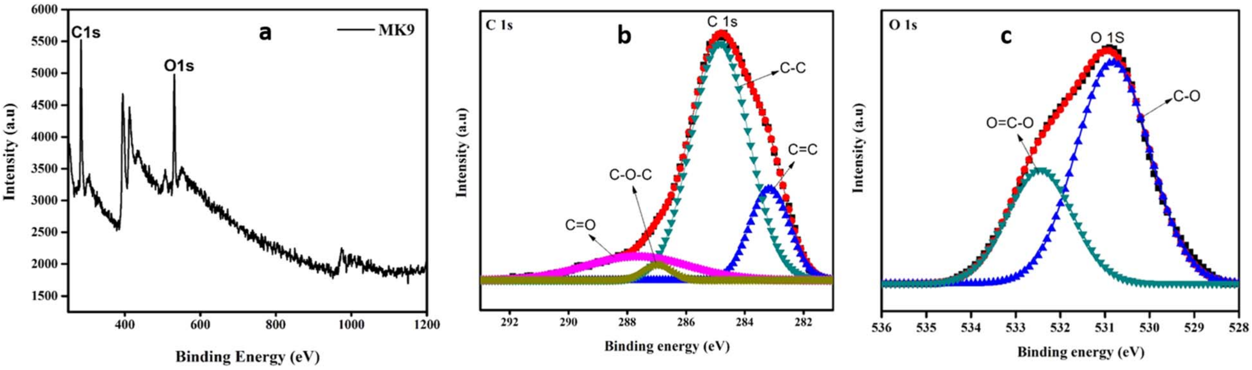

Fig. 6 XPS analysis of MK9 material (wide scan a) with deconvoluted spectrum of C 1s (b) and O 1s (c).

synthesized material and its potential utility in fields like adsorption, catalysis, and energy storage.

3.5. Electrochemical performance

Electrochemical measurements were carried out using an AUTOLAB M204 multichannel potentiostat/galvanostat (Netherlands). In the three-electrode setup, CV and GCD tests were performed within a potential range of 0 to −1.0 V. Similar CV and GCD analyses were conducted on the asymmetric device using a potential window of 0 to 1.4 V. All measurements were conducted in 3.0 M KOH and PVA-KOH gel electrolytes.

Eqn (1) was used to determine the gravimetric specific capacitance (C) for the electrodes in a three-electrode cell;[26]

$$C_{\mathrm{sp}} = \frac{I \times \Delta t}{m \times \Delta V} \tag{1}$$

in this equation, I represents the constant discharge current (A), Δt is the discharge duration (s), V denotes the voltage difference (V), and m refers to the total mass of the active material used.

$$C_{\mathrm{sp}} = 4\frac{I \times \Delta t}{m \times \Delta V} \tag{2}$$

Likewise, eqn (2) was applied to calculate the gravimetric specific capacitance (C) for asymmetric supercapacitors.

Here, C_{sp} represents the specific capacitance (F g^{-1}), m is the total mass of ZS/GP active material (g), I denotes the constant discharge current (A), Δt is the discharge duration (s), and ΔV is the voltage difference (V).

Eqn (3) and (4) are utilized to calculate the actual energy performance parameters of the devices, specifically the energy density (E) and power density (P).

$$E = \frac{C_{\mathrm{sp}} \times \Delta t^2}{7.2} \tag{3}$$

$$P = \frac{E \times 3600}{t} \tag{4}$$

3.6. Electrochemical investigation of MK7, MK8, MK9 and MK10 in 3 M KOH

The CV with a larger area shows that MK9 seems to hold more charges than its peers (Fig. 7a). The more or less rectangular profiles on all the electrodes demonstrate the viability of MK7, MK8, MK9, and MK10 as EDLC materials. GCD testing demonstrated a triangular and linear profile, both indicative of EDLC behavior[27] shown in Fig. 7b. The MK9 displayed longer discharge times, leading to better specific capacitance. It displayed a high specific capacitance of 205.8 F g^{-1} compared to MK7, MK8, and MK10, which displayed 107.9, 124.9, and 132.2 F g^{-1}, respectively. The FRA impedance of the MK electrodes is revealed by EIS analysis. All the MK electrodes showed very low impedance. An equivalent circuit was created to simulate the phenomena seen in the EIS analysis (inset in Fig. 7d). The series resistance shows the internal resistance of the solution with the lowest R_{ct} value recorded at 0.41 Ω and series resistance 0.4 Ω for the MK9 electrode, shown in Table 2. Because pyrolysis at

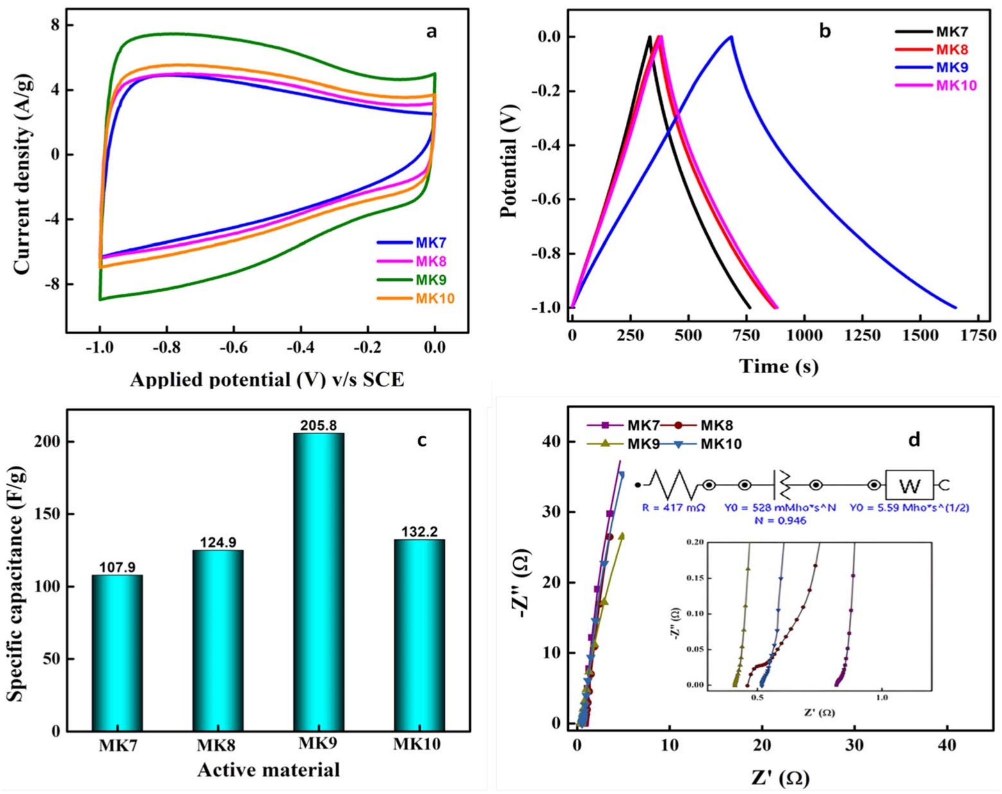

Fig. 7 Comparative CV of MK7, MK8, MK9, and MK10 samples at 50 mV s^{-1} scan rate (a), GCD tests of MK samples (b), specific capacitance at 0.25 A g^{-1} of all MK samples (c), and Nyquist impedance plot of samples (d); inset shows high-frequency region.

Table 2 Fitted equivalent circuit parameters for MK7, MK8, MK9, and MK10 electrodes

Electrode	R_s (Ω)	CPE(Q)/Ω s^N	C (mF)	W (Ω s$^{1/2}$)	χ^2
MK7	0.8	0.423 ($N = 0.98$)	434	4.51	0.06
MK8	0.47	0.452 ($N = 0.99$)	460	2.21	0.03
MK9	0.4	0.694 ($N = 0.94$)	672	5.58	0.02
MK10	0.5	0.528 ($N = 1.0$)	593	1.45	0.07

900 °C results in lower charge transfer resistance due to improved conductivity, higher porosity, and the presence of more active defect sites. In contrast, other temperatures lead to higher temperatures due to excessive graphitization, reduced porosity, and decreased surface functional groups.

Capacitive current due to the electrochemical double layer, denoted by the double-layer capacity C_{dl}, and Faraday current due to an electrochemical reaction, denoted by the charge transfer resistance R_{CT}, are both ways in which current can flow across the interface of the working electrode. As with the streamlined Randle's circuit, the projected EIS would be a semicircle up to this point. Capacitance is measured in units of constant phase element (CPE) rather than C_{dl}. MK7 electrode shows the semicircle at high frequencies (inset in Fig. 7d). Meanwhile, we see a vertical line for the others, ruling out Faraday current or charge transfer resistance. This corresponds perfectly to the form seen in the CV. That points to a species that is freely diffusing at the electrode. Because of the prolonged application of potentials at low frequencies, species depletion in the vicinity of the electrode becomes an issue. While the applied voltage remains the same, fewer species are converted, and less current flows when fewer species are in the electrode and the sample gap. This increase in impedance is what gets recorded during an EIS test. The Warburg impedance (W), a fictitious electrical component that appears solely in comparable circuits for electrochemical research, stands in for this rise. Nyquist plots reveal the Warburg impedance as a straight line at 45° to the abscissa. The depletion has a pronounced impact on the impedance at lower frequencies. Because of the reduced diffusion resistance, this line is less noticeable in MK electrodes.

3.7. Aqueous *vs.* organic electrolyte optimization of MK9

Aqueous electrolytes, such as KOH aqueous solution, offer several advantages over their organic counterparts, including higher ionic conductivity, lower cost, non-flammability, non-corrosiveness, enhanced safety, and ease of air assembly. However, a key limitation of aqueous electrolytes is their narrower potential window (approximately 1.2 V), which results in lower energy density and consequently restricts their widespread application. In symmetric supercapacitors, incorporating redox-active materials within the aqueous electrolyte can mitigate this issue by introducing additional redox interactions between the electrode and electrolyte, effectively increasing capacitance. Conversely, organic electrolytes often exhibit lower conductivity and higher cost, flammability, and toxicity, and offer a significantly wider operating voltage (up to 4 V). This wider potential window is a significant advantage, contributing to higher energy density. Commonly employed organic electrolyte solvents include acetonitrile (AN) and propylene carbonate (PC), while organic salts such as tetraethylphosphonium tetrafluoroborate and tetraethylammonium tetrafluoroborate ($\mathrm{TEABF_4}$) are also utilized in some organic electrolyte systems.

Organic electrolytes often operate in a greater potential window, between 2.5 and 2.8 V, as shown in Fig. 8b. Energy and power densities may be significantly improved with the higher operating cell voltage.[28] In an EDLC, both pore size and pore size distribution and specific surface area influence the specific capacitance. The accessibility of pores in an organic electrolyte is directly affected by the size of the cation and anion species and the interaction between ions and the solvent. Very tiny carbon particles may have a higher specific surface area if pores are present in the material, but this may come at the expense of the ability of a material to transport electrolyte ions. Because the pores are so tiny, more prominent organic ions have a more challenging time accessing the surface, which has a detrimental impact on specific capacitance. Therefore, achieving optimal specific capacitance necessitates a close match between the pore size of the carbon materials and the size of the electrolyte ions. We decided to use a $\mathrm{TEABF_4}$ solution in acetonitrile (AN) as the electrolyte. With a conductivity of 49 mS cm^{-1}, $\mathrm{TEABF_4}$ in AN solvent is among the best of its class.[28]

3.8. Electrochemical analysis of MK9 symmetric CR2032 cell

Since MK9 had a favourable electrochemical response in a three-electrode configuration, this material was selected for fabricating the cells and tested with different electrolytes to increase the device performance, as shown in Fig. 8. Benefits of organic solvents include a high dielectric constant, low volatility, and superior electrochemical stability. Organic electrolytes in supercapacitors can be costly and present safety concerns because organic solvents are flammable and volatile. Distinct CR2032 cells with MK9 symmetric electrodes with 6 different electrolytes were used to analyse the electrochemical response. CV analysis indicated that the cell with KOH electrolyte had a more stable and broader electrochemical window than other organic electrolytes (Fig. 8a). While the EMIM-BTI and BMP-BTI were able to operate reliably up to 3.0 V, the BMP-BTI AN and TEABF4/AN window was just 2.0 V. The greater CV area displayed by cells with KOH electrolyte indicated that the cells could store charges efficiently. A similar result was seen in GCD analysis with symmetric linear curves (Fig. 8b). While the cell with the KOH electrolyte had the highest specific capacitance 112.4 F g^{-1}, despite running at 3.0 V, the cell with BMP-BTI displayed a low specific capacitance of just 41.1 F g^{-1} (Fig. 8c). Although ILs allow for a larger voltage window to be used, many of them have significant limitations that make them impractical. These include their high viscosity, limited ionic conductivity, and high cost. Despite having a higher ionic conductivity than most typical ILs, the EMIM-BF4 electrolyte (14 mS cm^{-1} at 25 °C) conductivity is still much lower than that of TEABF4/AN (59.9 mS cm^{-1} at 25 °C), and 5.0 M aqueous KOH (600 mS cm^{-1} at 25 °C).[29–31]

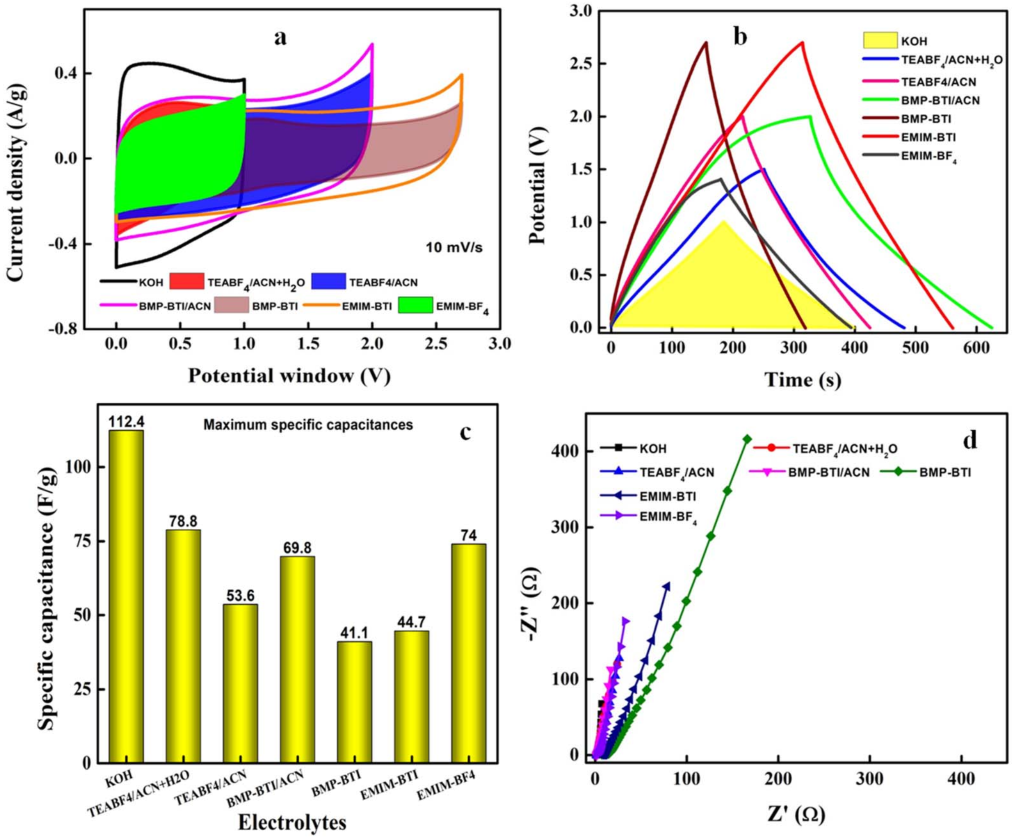

Fig. 8 Comparative CV of MK 9 coin cell device with different electrolytes (a), GCD tests at different electrolytes (b), the specific capacitance at different aqueous electrolytes (c), and Nyquist impedance plots (d), respectively.

The FRA impedance of the KOH electrolyte-based cell shows a proper semicircle arc compared to the other electrolytes. R_s and R_{ct} values are 0.83 and 2.8 Ω, respectively. The EMIM-BF_4 and BMP-BTI ACN electrolyte-filled cells displayed nominal resistance (Fig. 8d), with R_s values of 1.13 and 1.52 Ω, respectively. The BMP-BTI cell exhibited R_s of 7.236 Ω, in contrast. KOH is a strong electrolyte that fully dissociates into K^+ and OH^- ions in both aqueous and molten states. Its aqueous solution conducts electricity effectively due to the abundance of free ions. Any compound completely dissociating in an aqueous solution is classified as a strong electrolyte.

Electrolytes, including aqueous (KOH), organic (TEABF4-ACN), and ionic liquids (EMIM-BF_4, BMP-BTI, and EMIM-BTI) were used to create symmetric supercapacitors using MK9 as the active material. While using a KOH electrolyte, the specific capacitance reached 112.4 F g; however, extending operating voltages is necessary if the cell is employed in a wide range of applications and the energy density is to be increased; this cannot be done in an aqueous environment. We found that a voltage of 3.0 V could be maintained across the supercapacitor cell when EMIM-BTI was used as the electrolyte.

Fig. 9a presents the Bode plot, illustrating the frequency dependence of both phase angle (Φ) and impedance modulus (Z). Nyquist plots, commonly presented with equal scaling on both x and y axes, are used to assess impedance behaviour over a frequency range from 10^5 Hz (high-frequency) to 10^{-2} Hz (low-frequency).

The equivalent series resistance (ESR) is identified at the point where the impedance curve intersects the x-axis in the high-frequency region. For the cell using KOH aqueous electrolyte, the phase angle measured was approximately −84°, which is fairly close to the ideal capacitor value of −90°. This suggests near-ideal capacitive behaviour. However, the BMP-BTI organic electrolyte decreased the phase angle to −68° (Fig. 9a), indicating a deviation from ideal capacitance. The closer proximity to −90° observed with the aqueous KOH electrolyte and biomass-derived porous carbon likely arises from the superior ionic conductivity of the aqueous electrolyte and the efficient charge transfer facilitated by the inherent porous structure and surface functionalities of the biomass-derived CNS. These characteristics promote better ion accessibility and minimize diffusion limitations, leading to more ideal capacitive behaviour. In contrast, despite its wider potential window, the organic electrolyte may exhibit lower ionic conductivity and potentially less favourable interactions with the CNS material, resulting in a less ideal phase angle. A comparative summary is summarized in (Table 3) with key energy parameters of various biomass derived carbon based electrodes with those obtained in the present study.

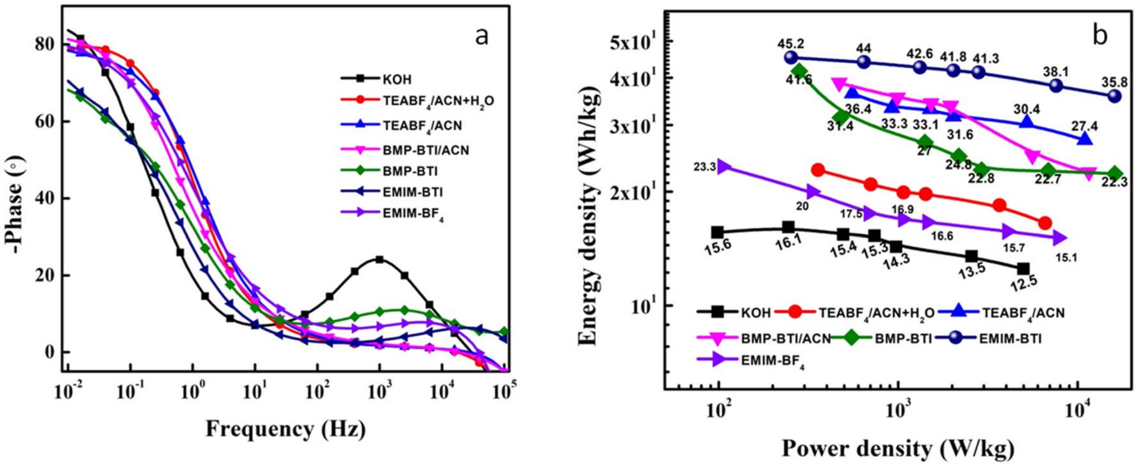

Fig. 9 Bodes phase angle plots (a), coulombic efficiency and capacitance retention of MK 9 device at different electrolytes (b).

Table 3 Comparison of key energy parameters of various biomass-derived carbon-based electrodes with those obtained in the current study

Precursor	Electrolyte	Voltage (V)	Energy density (W h kg^{-1})	Power density (W kg^{-1})	Specific capacitance (F g^{-1})	Ref.
Corn silks	MeEt$_3$NBF$_4$/PC	2.7	16.4	—	—	32
Lignin	Lignin-hydrogel	1.0	4.49	263	129.23	33
Areca palm leaves	PVA-Li$_2$SO$_4$	1.5	10.3	375	132	34
Pine cone	PVA-KOH	1.6	24.6	400	69	35
Recycled jute	KOH	0.9	21.0	182	51	36
Cherry blossom petals	H$_3$PO$_4$-PVA	1.0	NA	NA	154	37
Quinoa	6.0 M KOH	1.0	9.5	—	—	38
Seaweed	C$_2$H$_3$LiO$_2$	1.8	0.835 mW h cm^{-2}	2.25 mW cm^{-2}	185.7 mF cm^{-2}	39
Teak wood sawdust	PVA/KOH	1.7	27.1	178	67.2	40
	1.0 M KOH	1.3	20.5	148	75.2	
Platanus bark	TEABF$_4$-ACN	3.0	34.6	—	—	41
Mango kernels	**3.0 M KOH**	**1.2**	**12.32**	**5137**	**112.4**	**Present work**

While using a KOH electrolyte, the specific capacitance reached 112.4 F g^{-1}. However, extending operating voltages is necessary if the cell is employed in a wide range of applications and the energy density is to be increased. We found that a voltage of 3.0 V could be maintained across the supercapacitor cell when EMIM-BTI was used as the electrolyte. Although the capacitance decreased to 46 F g^{-1}, an impressive energy density of 44.78 W h kg^{-1} was achieved at a power density of 249 W kg^{-1}. Comparative tests between the fabricated cells and commercial supercapacitors revealed an outstanding electrochemical performance. Additionally, the coin cell using KOH as the electrolyte demonstrated an energy density of 12.32 W h kg^{-1} with a peak power density of 5137.86 W kg^{-1}, as shown in Fig. 8b. The electrochemical performance of typical supercapacitors could withstand 100 000 GCD cycles without significantly deteriorating their electrochemical performance. The manufactured cell also supplied enough energy to light a red LED (1.9 V) for around 15 minutes.

The viability and durability of MK9-CR2032 cells were evaluated. At 2.0 A g^{-1}, a cell with an aqueous electrolyte was put through 100 000 GCD cycles. Up until 66 000 cycles, the cell maintained a stunning coulombic efficiency of 100%. After that, we noticed a slow fall to 79.3% at the end of 100 000 cycles (Fig. 10a). Additionally, the efficiency of the cells with various electrolytes was compared. While the performance of the other electrolytes fluctuated, aqueous electrolyte efficiency remained constant. This emphasizes the need to select electrolytes with low viscosity and good conductivity. It is much simpler for EDL to develop when ionic mobility is high (as it is in water). This leads to improved Coulomb efficiency (Fig. 9a). After only ten minutes of charging at 1.0 A g^{-1}, a CR2032 cell could power a red LED light for 15 minutes (Fig. 10a, inset).

Fig. 10c and d shows the first and last 20 GCD cycles of the device. There is a natural decrease in capacitance retention over cycles; however, because capacitance retention has decreased, it need not imply that charge/discharge efficiency also has to decrease. Hence, the graph presents 100% reliable results. Total time taken for completion of 100 000 GCD cycles at 2 A g^{-1} was 49 days, 22 hours, 14 minutes, and 3 seconds.

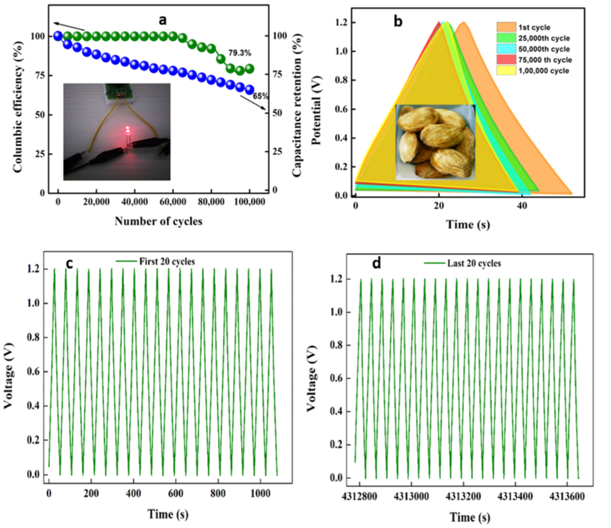

Fig. 10 Coulombic efficiency and capacitance retention of MK9 coin cell device at 3 M KOH electrolyte (a), stability/no. of cycles of MK9 device with KOH electrolyte (b). First and last 20 GCD cycles for stability testing (c and d).

4. Conclusion and future scope

Porous nanostructures were synthesized without using templates, catalysts, or activating agents; temperatures between 700 and 1000 °C from biomass sources. Maximum specific surface area by BET method was obtained when *Mangifera indica* kernels pyrolyzed at 900 °C was 1348.5 $m^2\ g^{-1}$. A CR2032-type symmetric supercapacitor was assembled utilizing different electrolytes. The effects of different electrolyte concentrations on capacitance and charge storage processes were also investigated. The KOH electrolyte-based coin cell was stable for 100 000 GCD cycles and has a maximum power density of 5137.86 W kg^{-1}, with an energy density of 12.32 W h kg^{-1}, and a C_{sp} of 112.4 F g^{-1}. Furthermore, the generated cell supplied sufficient energy for the illumination of a red LED for around 15 minutes. These results indicate that excellent potential of MK materials obtained from mango kernel wastes for high-performance supercapacitor applications.

Future research can explore the incorporation of heteroatom doping, such as nitrogen, sulphur, or phosphorus, to further enhance the capacitive behaviour and electrical conductivity of the mango kernel-derived carbon. Additionally, developing hybrid electrodes by combining the porous carbon with metal oxides or conducting polymers may significantly improve overall energy and power densities. Investigating alternative electrolytes, including ionic liquids or solid-state gel polymer electrolytes, could expand the operating voltage window and enable the fabrication of flexible or wearable super capacitor devices. Scaling up the synthesis process and integrating the material into full-cell super capacitor prototypes will be essential for assessing real-world applicability and device-level performance. Furthermore, conducting a detailed life cycle assessment (LCA) would provide insight into the environmental advantages of this biomass-derived material over conventional electrode materials. Finally, applying similar synthesis strategies to other agricultural wastes could diversify sustainable sources for high-performance carbon materials, further advancing green energy storage technologies.

Data availability

The data supporting this article has been included as part of the article.

Conflicts of interest

There are no conflicts to declare.

References

1 V. Molahalli, A. Shetty, K. Bijapur, G. Soman, A. Sharma, J. Joseph and G. Hegde, in *Green Energy and Technology*, Springer Nature Singapore, Singapore, 2023, pp. 1–39.
2 A. Aghmadi and O. A. Mohammed, *Batteries*, 2024, **10**, 141.
3 P. W. Mwaurah, S. Kumar, N. Kumar, A. Panghal, A. K. Attkan, V. K. Singh and M. K. Garg, *Compr. Rev. Food Sci. Food Saf.*, 2020, **19**, 2421–2446.
4 A. B. Stambouli and E. Traversa, *Renewable Sustainable Energy Rev.*, 2002, **6**, 433–455.
5 V. Molahalli, K. Chaithrashree, M. K. Singh, M. Agrawal, S. G. Krishnan and G. Hegde, *J. Energy Storage*, 2023, **70**, 108062.
6 S. Veeresh, H. Ganesh, Y. S. Nagaraju, M. Vandana, S. P. Ashokkumar, H. Vijeth, M. V. N. A. Prasad and H. Devendrappa, *Diamond Relat. Mater.*, 2021, **114**, 108289.
7 J. J Villora-Picó, J. González-Arias, F. M. Baena-Moreno and T. R. Reina, *Materials*, 2024, **17**, 565.
8 V. Molahalli, A. Sharma, K. Bijapur, G. Soman, N. Chattham and G. Hegde, *Mater. Today Commun.*, 2024, **38**, 108034.
9 X. Liu, L. Xue, Y. Lu, Y. Xia and Q. Li, *J. Electroanal. Chem.*, 2020, **862**, 114006.
10 L. Borchardt, M. Oschatz and S. Kaskel, *Mater. Horiz.*, 2014, **1**, 157–168.
11 B. Sakintuna and Y. Yürüm, *Ind. Eng. Chem. Res.*, 2005, **44**, 2893–2902.
12 C. Vix-Guterl, E. Frackowiak, K. Jurewicz, M. Friebe, J. Parmentier and F. Béguin, *Carbon*, 2005, **43**, 1293–1302.
13 H. Gege, X. Wu, Y. Hou and J. Cai, *Biomass Convers. Biorefin.*, 2020, **10**, 267–276.
14 C. D. S Wong, J. X. Yeoh, T. Wu, S. Manickam and C. H. Pang, *Chem. Eng. Process.*, 2022, **175**, 108908.
15 V. Molahalli, G. Soman, V. S. Bhat, M. S. Jyothi, U. Sirimahachai, S. Maradur, P. De Padova, N. Chattham and G. Hegde, *Nano Express*, 2024, **5**, 035006.
16 I. S. Choi, E. J. Cho, J. H. Moon and H. J. Bae, *Food Chem.*, 2015, **188**, 537–542.
17 A. Sharma, J. M. Shivanna, A. N. Alodhayb and G. Hegde, *Nanoscale Adv.*, 2024, **6**, 3199–3210.
18 S. H Paramesh, V. S. Ananthpur and N. Rajendraprasad, *J. Water Environ. Nanotechnol.*, 2024, **9**, 55–72.

19 J. Darabi, A. Ghiasvand and P. R. Haddad, *Talanta*, 2021, **233**, 122583.
20 M. S. Devi, T. D. Thangadurai, S. Shanmugaraju, C. P. Selvan and Y. I. Lee, *Adsorption*, 2024, **30**, 891–913.
21 T. Shang, Y. Xu, P. Li, J. Han, Z. Wu, Y. Tao and Q.-H. Yang, *Nano Energy*, 2020, **70**, 104531.
22 S. S. Diarra, *World Poult. Sci. J.*, 2014, **70**, 279–288.
23 S. Punia Bangar, M. Kumar and W. S. Whiteside, *Int. J. Biol. Macromol.*, 2021, **183**, 1807–1817.
24 T. Tesfaye, J. K. Johakimu, R. B. Chavan, B. Sithole and D. Ramjugernath, *Clean Technol. Environ. Policy*, 2018, **20**, 81–94.
25 P. S. Awodi, J. C. Ogbonna and T. N. Nwagu, *Heliyon*, 2022, **8**, e09707.
26 G. Soman, V. Molahalli, K. Sayeed, K. Pandey, B. B. Kulkarni and G. Hegde, *J. Energy Storage*, 2025, **111**, 115373.
27 V. Molahalli, G. Soman, V. S. Bhat, A. Shetty, A. Alodhayb and G. Hegde, *RSC Adv.*, 2024, **14**, 32314–32326.
28 C. Zhong, Y. Deng, W. Hu, J. Qiao, L. Zhang and J. Zhang, *Chem. Soc. Rev.*, 2015, **44**, 7484–7539.
29 M. Galiński, A. Lewandowski and I. Stępniak, *Electrochim. Acta*, 2006, **51**, 5567–5580.
30 R. Gilliam, J. Graydon, D. Kirk and S. Thorpe, *Int. J. Hydrogen Energy*, 2007, **32**, 359–364.
31 M. Armand, F. Endres, D. R. MacFarlane, H. Ohno and B. Scrosati, *Nat. Mater.*, 2009, **8**, 621–629.
32 J. Zhou, S. Yuan, C. Lu, M. Yang and Y. Song, *J. Electroanal. Chem.*, 2020, **878**, 114704.
33 J. H. Park, H. H. Rana, J. Y. Lee and H. S. Park, *J. Mater. Chem. A*, 2019, **7**, 16962–16968.
34 P.-A. Le, V.-T. Nguyen, S. K. Sahoo, T. Y. Tseng and K.-H. Wei, *J. Mater. Sci.*, 2020, **55**, 10751–10764.
35 F. Barzegar, A. Bello, J. K. Dangbegnon, N. Manyala and X. Xia, *Appl. Energy*, 2017, **207**, 417–426.
36 C. Zequine, C. K. Ranaweera, Z. Wang, P. R. Dvornic, P. K. Kahol, S. Singh, P. Tripathi, O. N. Srivastava, S. Singh, B. K. Gupta, G. Gupta and R. K. Gupta, *Sci. Rep.*, 2017, **7**, 1174.
37 X. Yu, Y. Wang, L. Li, H. Li and Y. Shang, *Sci. Rep.*, 2017, **7**, 45378.
38 Y. Sun, J. Xue, S. Dong, Y. Zhang, Y. An, B. Ding, T. Zhang, H. Dou and X. Zhang, *J. Mater. Sci.*, 2020, **55**, 5166–5176.
39 T. Ye, D. Li, H. Liu, X. She, Y. Xia, S. Zhang, H. Zhang and D. Yang, *Macromolecules*, 2018, **51**, 9360–9367.
40 V. S. Bhat, S. G. Krishnan, T. J. Jayeoye, T. Rujiralai, U. Sirimahachai, R. Viswanatha, M. Khalid and G. Hegde, *J. Mater. Sci.*, 2021, **56**, 13271–13290.
41 F. Yu, Z. Ye, W. Chen, Q. Wang, H. Wang, H. Zhang and C. Peng, *Appl. Surf. Sci.*, 2020, **507**, 145190.